ACS APPLIED MATERIALS & INTERFACES

Research Article

www.acsami.org

Subcellular Partitioning and Analysis of Gd^{3+}-Loaded Ultrashort Single-Walled Carbon Nanotubes

Brian D. Holt,[†] Justin J. Law,[‡] Patrick D. Boyer,[§] Lon J. Wilson,*[,‡] Kris Noel Dahl,*[,§,∥] and Mohammad F. Islam*[,†]

[†]Department of Materials Science and Engineering, [§]Department of Chemical Engineering, and [∥]Department of Biomedical Engineering, Carnegie Mellon University, Pittsburgh, Pennsylvania 15213, United States

[‡]Department of Chemistry and Smalley Center for Nanoscale Science and Technology, Rice University, Houston, Texas 77251, United States

Supporting Information

ABSTRACT: Magnetic resonance imaging (MRI) is of vast clinical utility, with tens of millions of scans performed annually. Chemical contrast agents (CAs) can greatly enhance the diagnostic potential of MRI, and ∼50% of MRI scans use CAs. However, CAs have significant limitations such as low contrast enhancement, lack of specificity, and potential toxicity. Recently developed, Gd^{3+}-loaded ultrashort single-walled carbon nanotubes, also referred to as gadonanotubes or GNTs, exhibit ∼40 times the relaxivities of clinical CAs, representing a potential major advance in clinically relevant MRI CA materials. Although initial cytotoxicity and MRI studies have suggested great promise for GNTs, relatively little is known regarding their subcellular interactions, which are crucial for further, safe development of GNTs as CAs. In this work, we administered GNTs to a well-established human cell line (HeLa) and to murine macrophage-like cells (J774A.1). GNTs were not acutely cytotoxic and did not reduce proliferation, except for the highest exposure concentration of 27 μg/mL for J774A.1 macrophages, yet bulk uptake of GNTs occurred in minutes at picogram quantities, or millions of GNTs per cell. J774A.1 macrophages internalized substantially more GNTs than HeLa cells in a dose-dependent manner, and Raman imaging of the subcellular distribution of GNTs revealed perinuclear localization. Fluorescence intensity and lifetime imaging demonstrated that GNTs did not grossly alter subcellular compartments, including filamentous-actin structures. Together, these results provide subcellular evidence necessary to establish GNTs as a new MRI CA material.

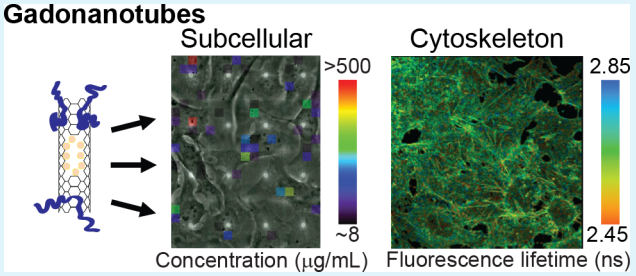

KEYWORDS: *actin, carbon nanotubes, chemical contrast agent, gadolinium, gadonanotubes, magnetic resonance imaging, Raman spectroscopy*

1. INTRODUCTION

Magnetic resonance imaging (MRI) is extremely important for clinical diagnosis of numerous prevalent pathologies ranging from cancer to congenital heart disease.[1] There are ∼25000 MRI scanners worldwide.[2] Therefore, improvements to the clinical utilization of MRI have the potential to significantly benefit human health. Although inherent MRI contrast is a function of both intrinsic and extrinsic parameters with some opportunity for controlling imaging performance, many diagnostic questions require the application of external chemical contrast agents (CAs).[2] Currently, the heavy-metal gadolinium ion (Gd^{3+}) is the basis for clinically used CA formulations.[1] Free Gd^{3+} is toxic,[3] so to minimize toxicity, the Gd^{3+} ion is typically chelated, which reduces the number of available water coordination sites and, in turn, reduces the performance (relaxivity) of Gd^{3+}.[4] Hence, CA materials that prevent the release of Gd^{3+} within the body while also maintaining or enhancing performance of CAs could represent a significant advance toward the potential development of more effective CAs for clinical use.

Recently, pioneering work has demonstrated that nanostructured carbon materials such as [C_{60}]fullerene and ultrashort single-walled carbon nanotubes (US-CNTs) internally loaded with Gd^{3+} ions exhibit relaxivities that are enhanced by ∼40-fold compared to that of the clinical standard of care (Magnevist, gadopentetate dimeglumine).[4] However, Gd^{3+}@C_{60} tends to form aggregates, which is the origin of much of their relaxivity enhancement.[5,6] As a result, when Gd^{3+}@C_{60} is disaggregated (individualized), the substantial enhancement advantage over the clinically available CAs is mostly lost. In contrast, Gd^{3+}@US-CNTs, hereinafter referred to as gadonanotubes or GNTs, maintain the ∼40-fold enhancement when individualized[7,8] and, hence, are a highly

Received: January 16, 2015
Accepted: June 22, 2015
Published: June 22, 2015

DOI: 10.1021/acsami.5b04851
ACS Appl. Mater. Interfaces 2015, 7, 14593−14602

desirable candidate as a new MRI CA material. However, developing GNTs for clinical applications requires extensive and careful studies of their interactions with cells and biological tissue.

Previous studies with GNTs have shown that the Gd^{3+} ions remain sequestered within the US-CNTs,[9] and any free Gd^{3+} remaining after GNT synthesis was removed before use in cellular experiments, preventing cytotoxicity from Gd^{3+}.[4,10] Preliminary studies of GNTs stabilized by Pluronic F108 (PF108)[10−12] and other Gd^{3+}-incorporated carbon nanostructured materials[13−15] have reported cytocompatibility. For instance, biocompatibility studies of single-walled CNTs (SWCNTs) synthesized with gadolinium nanoparticles[16] with NIH-3T3 fibroblasts revealed minimal alterations to cellular viability, membrane integrity, apoptosis, and cell cycle that only became significant after 48 h of cellular exposure to at least 10 μg/mL.[13] When dispersed in water and intravenously injected into rats, aggregates of these gadolinium-containing SWCNTs were detected in the lung, liver, brain, and spleen, but there was neither inflammation nor organ damage for at least 30 days and no change in liver gene expression occurred within a day after injection.[17] Furthermore, intraperitoneal injection of very high concentrations of US-CNTs led to granulomas containing aggregates of US-CNTs, whereas US-CNTs that remained dispersed were renally cleared.[18] These in vitro and in vivo studies suggest that, at appropriate doses, Gd^{3+}-containing CNTs could be safely administered, yet the cellular uptake and subcellular partitioning of well-dispersed US-CNTs and GNTs remain largely unexplored.

In this work, we have investigated the effects of GNTs on the human cell line HeLa and murine macrophage-like cells, J774A.1. We determined the subsequent subcellular distribution of GNTs to explore the appropriateness for further development of GNTs as a new MRI CA material. GNTs were individually dispersed in water with PF108 or bovine serum albumin (BSA) to determine potential differences in interactions of the GNTs with cells arising from the dispersing agent (biocompatible polymer versus protein). We used cell enumeration and late apoptosis assays to quantify the effects of the dispersing agent and Gd^{3+} loading within the US-CNTs on cellular proliferation and viability. Unlike a few previous studies that relied on Gd^{3+} ion concentration to quantify cellular internalization,[10] we utilized the CNTs' Raman signature to determine bulk cellular uptake and map the subcellular distribution of both US-CNTs and GNTs as a function of exposure time and concentration. Confocal fluorescence imaging and fluorescence lifetime imaging microscopy were also used to probe the GNT subcellular partitioning and its effects on cellular structures. Taken together, the analyzed data of this study provide cellular and subcellular information that is needed to advance the development of GNTs as a safe clinical MRI CA.

2. EXPERIMENTAL SECTION

2.1. CNT Dispersions. SWCNTs produced by the electric arc discharge method were purchased from Carbon Solutions, Inc. The nanotubes were fluorinated and cut by pyrolysis according to published methods.[19] The shortened US-CNTs were purified by treatment with hydrochloric acid, debundled by reduction with metallic sodium, and oxidized by brief exposure to nitric acid. GNTs were produced by aqueous ultrasonication of the shortened nanotubes in a solution of gadolinium chloride for 1 h, followed by filtration and washing with deionized water.[8] GNTs prepared by this method had Gd^{3+} loadings of <3% by weight.[8]

Both US-CNTs and GNTs were dispersed in ultrapure water using either Pluronic F108 triblock copolymer (PF108, BSAF) or bovine serum albumin (BSA, Sigma-Aldrich) according to previously established protocols.[20−22] Briefly, we began by mixing CNTs and the dispersing agents in water at a CNT concentration of 0.1 wt % with a weight ratio between the CNTs and the dispersing agents of 1:10. The mixture (typically ∼3 mL) was sonicated using a probe tip (Fisher Scientific, Sonic Dismembrator model 100, 3-mm probe tip) that applied 6 W of power for 2 h. CNT dispersions with BSA were centrifuged for 7 min at 21000*g*,[20,21] whereas dispersions with PF108 were centrifuged for 30 min at 21000*g*.[23] Supernatants were carefully decanted, optically characterized, and UV-sterilized for 1 h before cellular experiments.

2.2. Absorbance and Raman Spectroscopies of CNTs. UV−vis−NIR absorbance spectroscopy was performed using a Varian Cary 5000 spectrophotometer. CNT concentration was determined using a known absorbance coefficient at 930 nm of 2.6 (absorbance mL)/(mg mm).[20−24] Raman spectroscopy and imaging was performed using an inverted confocal Raman microscope (inVia confocal Raman, Renishaw). A 50× air objective with a 0.75 numerical aperture (NA) was typically used for bulk uptake measurements, and a 100× oil-immersion objective with 1.4 NA was used for Raman mapping. Bulk uptake measurements were performed on cell lysates (see section 2.6). Mapping experiments were performed on fixed cells mounted on microscopy slides (see section 2.5 for fixation methods). Typical Raman maps were acquired with a ∼5-μm step size and ∼10-s integration time for HeLa cells and with a ∼1-μm step size and ∼1-s integration time for J774A.1 macrophages; ∼10 mW of 785 nm (1.58 eV) laser intensity; and concatenation of multiple images to form a larger, aggregate field of view. Control of Raman spectroscopy and imaging acquisition parameters was performed in WiRE 3.4 software (Renishaw). To determine bulk uptake and spatially delineated uptake of CNTs in cells from Raman spectra and Raman mapping, respectively, the Raman G-band intensity of the nanotubes was correlated to the CNT concentration. To this end, the concentration of the starting stock solution was determined using UV−vis−NIR absorbance spectroscopy and the absorbance coefficient. We then performed serial dilutions and measured the nanotube Raman G-band intensity from these dispersions to create a standard curve of Raman G-band intensity versus nanotube concentration. Details on how to make such a standard curve are provided elsewhere.[21]

2.3. Electron Microscopy of GNTs. The structure of GNTs has been previously reported,[8] and we further characterized this batch of GNTs using high-resolution transmission electron microscopy (TEM), energy-dispersive X-ray (EDX) spectroscopy, and electron energy loss spectroscopy (EELS) using an FEI Titan G2 80-300 electron microscope.

2.4. CNT Stability. To assess the stability of PF108- and BSA-stabilized CNT dispersions under conditions similar to those encountered during cell experiments, initial CNT dispersions at ∼100 μg/mL were diluted in either ultrapure water (resistivity of 18.3 MΩ·cm, total oxidizable carbon content of 3 ppb) or complete cell culture medium (osmotic concentration of ∼350 mOsm/L, which is similar to that of whole blood (∼285 mOsm/L[1]) and ∼10 times less oncotic pressure than whole blood[25]) to 3 μg/mL and incubated at 5% CO_2 and 37 °C for 48 h, and then UV−vis−NIR absorbance spectra before and after incubation were collected and compared. Further, we also examined the stability of all CNT dispersions after storage for 3 weeks at 4 °C using UV−vis−NIR absorbance spectroscopy.

2.5. Cell Culture and Biocompatibility. HeLa cells were maintained at 5% CO_2 and 37 °C in complete cell culture medium: Dulbecco's Modified Eagle Medium (1000 mg/L glucose, 4.0 mM L-glutamine, and 110 mg/L sodium pyruvate; Thermo Scientific) supplemented with 10% v/v fetal bovine serum (FBS; Life Technologies) and 1% v/v penicillin/streptomycin (Life Technologies). J774A.1 murine macrophage-like cells were maintained at 5% CO_2 and 37 °C in complete cell culture medium: Dulbecco's Modified Eagle Medium (4500 mg/L glucose, 4.0 mM L-glutamine, and no sodium pyruvate; Thermo Scientific) supplemented with 10% v/v FBS and 1% v/v penicillin/streptomycin (Life Technologies). For CNT

DOI: 10.1021/acsami.5b04851
ACS Appl. Mater. Interfaces 2015, 7, 14593−14602

experiments, HeLa cells were seeded at 3.0×10^4 cells/cm^2, or J774A.1 macrophages were seeded at 2.0×10^4 cells/cm^2 and incubated for 24 h. For imaging experiments, cells were seeded on sterilized #1.5 glass coverslips (Fisher). Then, the medium was exchanged, and the CNTs were diluted to the indicated concentration in fresh cell culture medium and retained for the duration of the experiment. To account for the dilution of nutrients, additional FBS was also added at 10% of the volume of CNTs (or controls) added.

For fixed cell imaging, cells were fixed in 3.7% formaldehyde, permeabilized with 0.2% v/v Triton X-100, and labeled with rhodamine phalloidin at 0.165 μM (Life Technologies) and 4′,6-diamidino-2-phenylindole at 0.25 μg/mL (DAPI; Life Technologies). For proliferation and viability analysis, the medium was aspirated, the cells were washed once with 1 × PBS, the cells were incubated for ∼30 min in Leibovitz medium with Hoechst 33342 at 0.25 μg/mL (Life Technologies) and propidium iodide (PI) at 500 nM (Life Technologies), the medium was exchanged for 1 × PBS, and the sample was then rapidly fluorescently imaged using 20× magnification. Proliferation was calculated as percentage of control cells, and viability was calculated as percentage of PI(+) cells for each condition.

Calcium levels were assessed using calcein. HeLa cells were seeded at 3.0×10^4 cells/cm^2, and J774A.1 cells were seeded at 2.0×10^4 cells/cm^2 and incubated for 24 h. Then, the medium was changed, and the cells were exposed to CNTs at 9 μg/mL. After 24 h of exposure, the CNT-laden medium was aspirated, the cells were washed with PBS, and the cells were exposed to calcein (for calcium) at 1 μM and Hoechst 33342 (for DNA) at 0.25 μg/mL dissolved in PBS for 30 min. The staining solution was then aspirated, the cells were washed with PBS, and the cells were exposed to Triton X-100 at 0.2% v/v in PBS to minimize the effects of cellular compartmentalization. Calcein and Hoechst 33342 fluorescence were assessed using a fluorescence microplate reader. Data are presented as calcein signal per cell (dividing calcein fluorescence by Hoechst 33342 fluorescence), normalized to the control.

2.6. CNT Uptake. Bulk CNT cellular uptake was determined according to previously described methods.[20−22,26] Briefly, after exposure to CNTs, the CNT-laden medium was aspirated from the cells' wells, the cells were washed with 1 × PBS, and the number of cells was determined before the cells were lysed. Total cell number was assessed by both imaging and protein assay. Before imaging, cells were labeled with Hoechst 33342 (Life Technologies) to label nuclei to create stark contrast for automated image processing. Multiple fields of view were imaged at 20× magnification, and total cell count was found by extrapolating the cells per total imaged area to the area of the entire well. Also, a protein assay was performed. Cells were analyzed by both their absorbance at 280 nm and their absorbance at 595 nm for a Coomassie (Bradford) Protein Assay (Pierce Biotechnology, Thermo Scientific) related to the appropriate standard curve. After the cell count had been performed, the cells were lysed with cell lysis buffer according to the manufacturer's recommendations (Cell Signaling Technologies), sonicated using a probe tip, placed into a 24-well glass-bottom dish, and subjected to confocal Raman spectroscopy.

2.7. Widefield and Confocal Imaging. Low-magnification widefield imaging was performed on an inverted Leica DMI 6000B fluorescence and light microscope with a 20× phase-contrast air objective with 0.4 NA, a Leica DFC350 FX charge-coupled device (CCD), and Leica Application Suite Advanced Fluorescence (LAS AF) software. High-magnification widefield imaging was performed on an inverted Leica DMI 4000B fluorescence and light microscope with a 100× phase-contrast oil-immersion objective with 1.4 NA and an Imperx IPX-VGA210 CCD.

Confocal fluorescence microscopy was performed on an inverted Leica TCS SP5 laser scanning multiphoton confocal fluorescence microscope with a 100× oil-immersion objective with 1.4 NA. Confocal Z-stacks were acquired with an $X-Y$ pixel resolution of 1024 × 1024, a Z step size of ∼0.1 μm, a 700 Hz scan rate, and multiple frame averaging. Confocal maximum projections were created in LAS AF software.

2.8. FLIM. Time-correlated single-photon-counting fluorescence lifetime imaging microscopy (FLIM) was performed on the above-described Leica TCS SP5 confocal microscope using an 80 MHz pulsed Ti-sapphire laser (Chameleon, Coherent) (multiphoton excitation) and an SPC-830 photon-counting device (Becker & Hickl GmbH), as described previously.[27,28] Briefly, FLIM images were acquired at 256 × 256 pixels for at least 300 s to maximize total acquired photons to enable a valid fit to a two-exponential decay, if appropriate.[29,30] Pixel-by-pixel exponential fits and FLIM images were generated in SPCImage software (Becker & Hickl GmbH). Quantification of average FLIM parameters (e.g., fluorescence lifetime, τ, and goodness of fit, χ^2) was performed in MATLAB using in-house code.[27,28]

3. RESULTS AND DISCUSSION

3.1. Materials Characterization and Dispersion Stability. We characterized the structure of as-produced GNTs by high-resolution TEM and determined elemental composition using EDX spectroscopy and EELS (Figure S1, Supporting Information). High-resolution TEM revealed the presence of SWCNTs with side-wall defects, as expected for these GNTs (Figure S1A, Supporting Information). EDX spectra showed strong peaks for carbon (C), nickel (Ni), and copper (Cu), in addition to peaks for Gd (Figure S1B, Supporting Information). Quantification of the EDX data revealed that the as-produced GNTs contained 0.37 ± 0.01 wt % Gd (Figure S1C, Supporting Information). EELS-based imaging further corroborated that Gd was present in the SWCNT structure (Figure S1D, Supporting Information). A representative EELS spectrum showed that the Gd N edge was weak but present (Figure S1E, Supporting Information). Overall, the combination of high-resolution TEM, EDX spectra, and EELS confirmed the GNT structure.[8] We note that the EDX and EELS spectra showed that the as-produced GNTs contained a substantial weight percentage of metallic impurities (Figure S1B,C, Supporting Information); some of the metal impurities likely originated from residual metal catalysts from CNT synthesis. However, the GNTs that were administered to cells were centrifuged at 21000g for 30 min (7 min) after being dispersed in aqueous solvent with PF127 (BSA), which likely removed nearly all metallic impurities. Our EDX and EELS spectra suggest that, to employ GNTs for MRI applications, a suitable purification process will need to be developed that removes undesired metallic impurities.

We characterized nanotube concentration, structural integrity, and dispersion state (i.e., whether the nanotubes were individually dispersed or existed in bundles) of the PF108- and BSA-stabilized US-CNT and GNT dispersions using optical absorbance and Raman spectroscopies (Figure S2, Supporting Information). The spectra were similar to those previously reported for similarly prepared US-CNTs and GNTs.[31] Details are provided in the Supporting Information.

CNT dispersion stability in physiologically relevant media is important for biological applications, as aggregates lack the desirable properties of individualized SWCNTs, have altered cellular interactions, might occlude the vasculature, and might become too large for renal clearance.[32] Unfortunately, defects in GNTs make it difficult to determine the quality and stability of the dispersions. Nevertheless, here, we qualitatively characterized the quality of our dispersions and how that quality changed as a function of time and exposure to complete cell culture medium, which has osmotic and oncotic strengths similar to those of blood.

PF108- and BSA-dispersed US-CNTs and GNTs were diluted in either ultrapure water or complete cell culture medium and incubated for 48 h at 37 °C and 5% CO_2 (i.e.,

DOI: 10.1021/acsami.5b04851
ACS Appl. Mater. Interfaces 2015, 7, 14593−14602

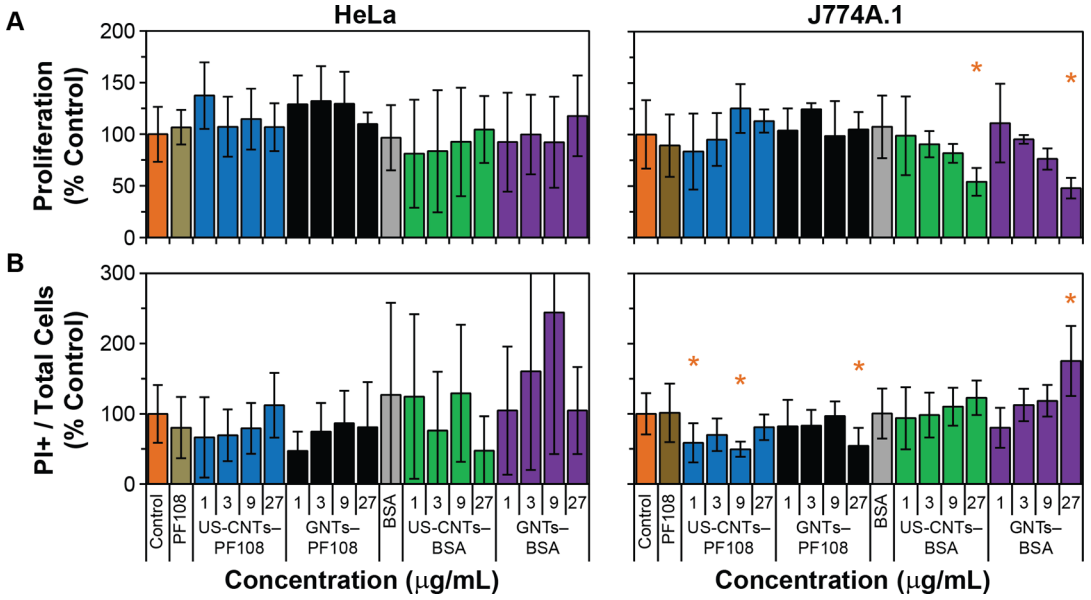

Figure 1. Effects of PF108- and BSA-dispersed US-CNTs and GNTs on HeLa and J774A.1 cellular proliferation and viability. (A) Proliferation measured by cell enumeration assay. (B) Viability measured by propidium iodide exclusion. Cells were exposed to the indicated conditions for 24 h. Asterisks (*) indicate a p value of <0.05 for a t test of the indicated conditions compared to the control. n = 3 for HeLa with error bars that are the propagated standard error of the mean. n = 4 for J774A.1 with error bars that are the sample standard deviation of the mean.

standard cell culture conditions). Because of defects in the structure of US-CNTs that enable Gd^{3+} loading, the van Hove peaks in the optical spectra were nearly nonexistent or very broad, and it was difficult to reliably determine dispersion quality from nanotube absorbance spectra. Still, such spectra from before and after ~100× dilution in either ultrapure water or complete cell culture medium and incubation for 48 h at 37 °C showed minor changes (Figure S3A,B, Supporting Information), as confirmed by quantification of the root-mean-square difference between the normalized spectra of the initial samples and the same of the diluted samples (Figure S3C, Supporting Information). However, after storage for 3 weeks at 4 °C, the PF108-dispersed CNTs aggregated, and all water-dispersed samples visibly aggregated (Figure S3D, Supporting Information).

These results demonstrate that aggregation of freshly prepared GNTs in physiologically relevant medium was minimal, avoiding the negative effects from aggregated CNTs. Further, renal clearance of rodlike nanostructures is possible for diameters of <6 nm[32] and has been experimentally demonstrated for SWCNTs.[18,33] Because GNTs remain stably dispersed and dispersion is important for clearance,[18] they might be renally clearable, potentially allowing for the safe use of GNTs as an MRI CA material followed by elimination of GNTs from the body.

3.2. Proliferation and Viability. An important consideration for the development of GNTs for clinical applications is potential toxicity, as free Gd^{3+} inhibits calcium channels and is highly toxic[3] and US-CNTs themselves could negatively affect cells. Previous studies have shown that Gd^{3+} ions remain sequestered within the US-CNTs upon physiological challenge[9] and that GNTs and similar gadolinium-containing nanostructured carbon materials are cytocompatible.[4,9−13] However, investigations typically did not focus on the dispersing agent or the potential alteration to the nanomaterial interface. Therefore, we dispersed the US-CNTs and GNTs with PF108, which is cytocompatible and has previously been used to disperse GNTs. In addition, we dispersed nanotubes in BSA, which is also cytocompatible and which we previously used to disperse other types of SWCNTs.[20−22] Note that albumin is the most prevalent serum protein and, thus, is most likely to contact and potentially alter a GNT dispersion administered to the body.

We studied the effects of PF108- and BSA-stabilized US-CNTs and GNTs on cellular growth and viability by administering the CNTs to HeLa cells and J774A.1 macrophages at concentrations ranging from 1 to 27 μg/mL and quantifying cell proliferation (cell enumeration assay) and acute toxicity (exclusion of the cellular-membrane-impermeable propidium iodide, PI). We chose 27 μg/mL as an upper concentration limit because it corresponds to a substantially larger mass of GNTs than needed to obtain sufficient contrast for potential MRI applications.[4] We observed no change in HeLa cellular proliferation relative to untreated control cells for any conditions (Figure 1A). However, there were statistically significant reductions in J774A.1 macrophage proliferation for the BSA-dispersed CNTs at 27 μg/mL. The US-CNTs and GNTs with either of the dispersing agents did not increase the percentage of PI(+) HeLa cells, which suggests that neither type of CNTs is acutely cytotoxic (Figure 1B) to HeLa cells. However, the highest exposure concentration of BSA-dispersed GNTs significantly increased the percentage of PI(+) J774A.1 macrophages. We suggest that these reductions in J774A.1 macrophage proliferation and viability resulted from the substantially higher internalization of BSA-dispersed CNTs by the J774A.1 macrophages, as described in the following sections. Overall, the US-CNTs and GNTs, dispersed with either BSA or PF108, were not toxic and reduced proliferation or viability for only the highest concentration exposures of BSA-dispersed CNTs to J774A.1 macrophages. These results are consistent with results obtained for similar GNTs and other processed SWCNTs.[21,23,26]

We next examined calcium levels in cells by exposing HeLa and J774A.1 cells to US-CNTs or GNTs and quantifying the fluorescence of the Ca^{2+}-sensitive dye calcein. There was no

DOI: 10.1021/acsami.5b04851
ACS Appl. Mater. Interfaces 2015, 7, 14593−14602

statistical change in Ca^{2+} level per cell compared to the control (Figure S4, Supporting Information), confirming that Gd^{3+} was sequestered within the nanotubes. Overall, neither US-CNTs nor GNTs altered the overall cellular Ca^{2+} levels in HeLa cells and J774A.1 macrophages at least up to the maximum tested concentration of 27 μg/mL.

3.3. Quantification of Cellular Uptake. Previous studies utilized Gd^{3+} exclusively to quantify nanotube uptake into cells.[10−13,34] Unfortunately, this method can underestimate the nanotube concentration in cells if the Gd^{3+} loading in the US-CNTs is highly heterogeneous. Furthermore, this approach cannot be utilized to compare and contrast US-CNT uptake in cells relative to GNT uptake. Indeed, cellular uptake of US-CNTs as compared to GNTs remains unexplored to date. We therefore utilized the unique intense Raman features of US-CNTs and GNTs to quantify their mass per cell using methods previously developed by our group.[20,21] This approach allowed us to both determine the cellular uptake of US-CNTs and compare it to the GNT uptake into cells.

Time-dependent measurements demonstrated that a significant amount (~1 pg/cell) of CNTs was associated with HeLa after 10 s of exposure to a concentration of 9 μg/mL (Figure 2A). Generally, uptake increased monotonically with time; however, the rate of uptake decreased until ~0.5 h, after which the uptake per cell was similar. Long-time (24-h) HeLa cell uptake showed little dependence on exposure concentrations, with a bulk average uptake of ~3 pg/cell over an exposure concentration range of 1−27 μg/mL (Figure 2B, top). In contrast, J774A.1 macrophages exhibited a dose-dependent uptake for all conditions (Figure 2B, bottom). Neither CNT type (US-CNTs or GNTs) had a substantial effect on time- or concentration-dependent uptake: The increase of GNT uptake compared to US-CNT uptake was (26 ± 34)% for HeLa cells and (9 ± 19)% for J774A.1 macrophages (mean ± standard error of the mean). However, the dispersing agent had a substantial effect on uptake, as there was a (60 ± 26)% increase in HeLa cell uptake and a (75 ± 26)% increase in J774A.1 macrophage uptake of BSA dispersions compared to PF108 dispersions.

Unlike for slightly longer SWCNTs (~145-nm),[21,26] uptake of US-CNTs and GNTs into HeLa cells had little dependence on CNT exposure concentration. Ultimately, this led to a bulk HeLa cell uptake of ~3.3 ± 1.4 pg/cell regardless of treatment level. These results were similar to other published cellular uptake values of GNTs[10−13] and are discussed in more detail in the Supporting Information.

For clinical MRI applications, intravenous or oral administration of GNTs would expose epithelium to GNTs. These cells might internalize less GNTs than HeLa and J774A.1 macrophage cells, potentially allowing for more rapid renal clearance. Previous studies have shown that cells can expel internalized CNTs;[22,35−38] thus, cells might be able to "recover" from exposure to GNTs through expulsion of internalized GNTs, although more studies are needed to understand the long-term cellular fate of GNTs both in vitro and in vivo. Ultimately, uptake might affect contrast for clinical MRI applications, and more studies are needed to understand these effects.

3.4. Subcellular Localization. Understanding the long-term subcellular localization of GNTs is crucial for verifying the cytocompatibility of GNTs. Although some studies have evaluated subcellular localization of GNTs using bright-field or transmission electron microscopies,[10,12,13,17,34] these modalities have some limitations. Contrast in bright-field microscopy is generated from absorbance; therefore, only very large local concentrations of GNTs can be detected, and there is no specificity for GNTs. Although transmission electron microscopy can provide nanometer-level resolution, imaging individual SWCNT within cells is challenging because of a lack of contrast between SWCNTs and intracellular materials. Resonant Raman[39] imaging allows for high sensitivity and specificity for SWCNTs while achieving diffraction-limited spatial resolution. Hence, Raman images of GNT intensity coregistered with optical images of cellular features are useful for determining GNT subcellular distribution. One study showed a Raman map of GNT intensity coregistered with a bright-field image of a NIH-3T3 cell.[13] Unfortunately, only one cell was included, and the local GNT concentration was not determined.

Therefore, we performed Raman imaging of HeLa cells and J774A.1 macrophages after exposure to PF108- and BSA-stabilized US-CNTs and GNTs to ascertain the intracellular distribution of the CNTs. Heat maps based on the G-band intensity of the CNTs revealed perinuclear subcellular local-

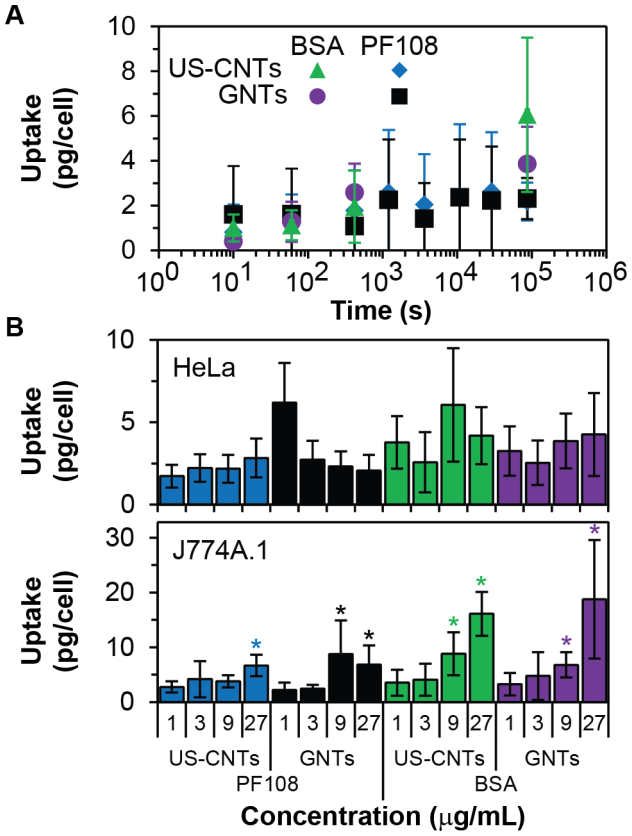

Figure 2. Quantification of cellular uptake of CNTs. (A) Time-dependent HeLa cell uptake for PF108- and BSA-dispersed US-CNTs and GNTs from 10 s to 24 h (time points at 10 and 60 s; 7, 20, and 60 min; and 3, 8, and 24 h). All data are shown for a 9 μg/mL cellular exposure concentration. n = 2 with error bars that are the propagated standard deviation for CNT mass and cell number. (B) Long-time (24-h), dose-dependent uptake into HeLa cells (top) and J774A.1 murine macrophages (bottom) as a function of concentration. Asterisks (*) indicate a p value of <0.05 for the indicated conditions compared to uptake with 1 μg/mL exposure. n = 3 for HeLa cells with error bars that are the propagated standard deviation for CNT mass and cell number. n = 5 for J774A.1 macrophages with error bars that are the propagated standard deviation for CNT mass and cell number.

DOI: 10.1021/acsami.5b04851
ACS Appl. Mater. Interfaces 2015, 7, 14593−14602

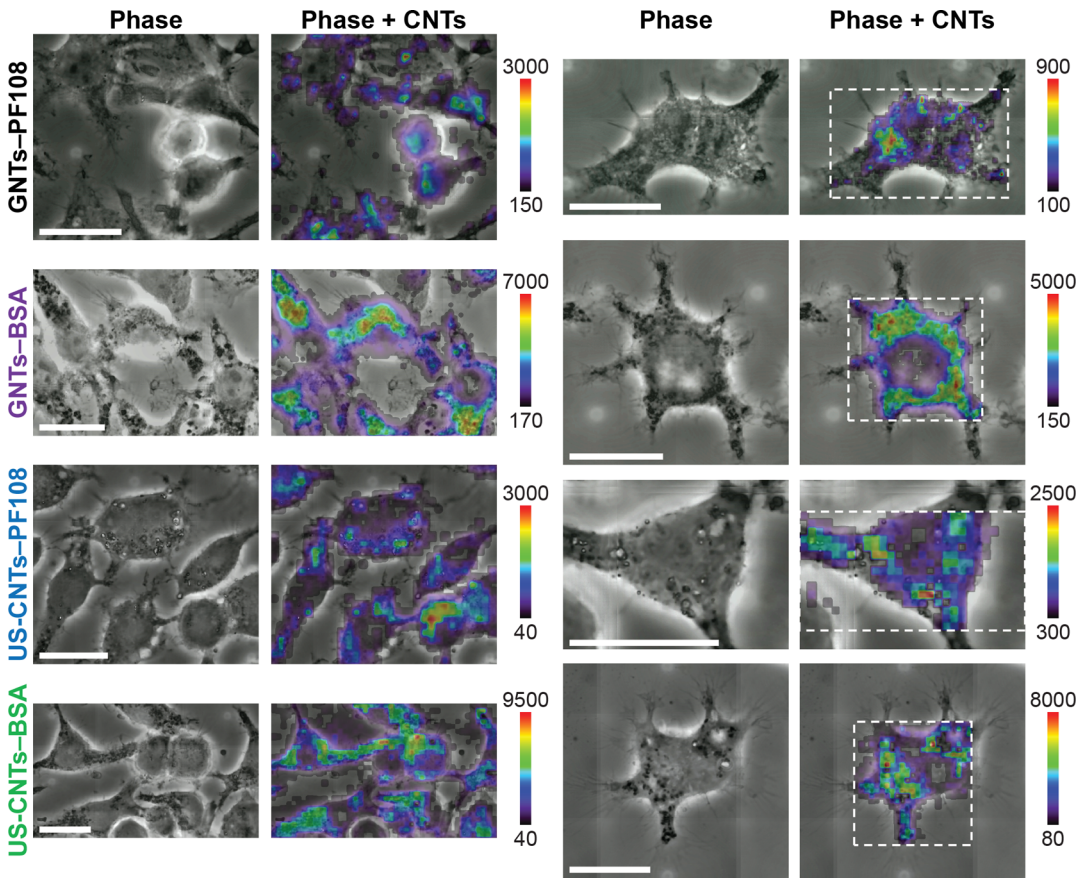

Figure 3. Raman mapping of CNT subcellular distribution within J774A.1 macrophages. Raman mapping of CNT G-band intensity coregistered to high-resolution phase-contrast images demonstrated perinuclear subcellular localization. The left-side fields of view show many cells per condition, demonstrating that the subcellular localization is consistent across the cell population, and the right-side fields of view zoom in on individual cells to clearly show subcellular localization. All samples were J774A.1 macrophages exposed to 10 μg/mL of CNTs for 24 h. Scale bars are 20 μm, and the color bar indicates the local CNT concentration. The white, dashed boxes on the right indicate the region that was imaged with Raman spectroscopy. n > 10 cells for each condition.

ization within J774A.1 macrophages (Figure 3). For HeLa cells, CNT uptake was substantially less than that for J774A.1 macrophages, preventing the acquisition of high-spatial-resolution heat maps. However, Raman imaging revealed subtle differences between cells exposed to PF108- and BSA-dispersed CNTs (Figure S5, Supporting Information). Cells that were exposed to PF108-dispersed CNTs exhibited discrete regions of high concentrations of CNTs that coregistered with regions of high indexes of refraction in phase-contrast imaging. The CNT concentrations in these high-concentration regions were more than 50 times more concentrated than the exposure concentration. For cells exposed to BSA-dispersed CNTs, these regions were absent from both the G-band-based heat map and phase images, and CNT intensity was more uniformly distributed throughout the cells.

It was previously shown that serum proteins could displace PF108 on SWCNTs after PF108-dispersed SWCNTs were added to blood in an in vivo rabbit model.[40] Other studies have shown a fast exchange between bound Pluronic F127 adsorbed on SWCNTs with free Pluronic F127 in solution.[41] Further, we observed long-term aggregation of PF108-stabilized CNTs in the cell culture medium. Therefore, we suggest that there might have been desorption of PF108 upon dilution in complete cell culture medium that resulted in some CNT bundling, manifesting as small aggregates associated with the HeLa cells. However, Raman imaging of CNTs within J774A.1 macrophages revealed a similar, perinuclear subcellular localization without the overt PF108-dispersed CNT aggregates on the cell membrane. Because macrophages phagocytose, aggregates could be internalized and trafficked to the perinuclear regions. Thus, macrophages do not have distinct aggregates on their cell membrane. Although desorption was also possible for BSA,[42] we did not observe any subcellular aggregates for BSA-dispersed CNTs or substantial long-term bundling in vitro.

Although we did not fluorescently label nuclei, high-resolution phase-contrast imaging was sufficient to identify most nuclei. Unlike functionalized [C_{60}]fullerene,[43] neither PF108- nor BSA-dispersed CNTs preferentially colocalized within the nucleus, for either HeLa or J774A.1 macrophage cells. These extranuclear subcellular localizations were similar to results obtained for Pluronic F127- and BSA-dispersed SWCNTs with lengths of ~145 nm.[20−22,26]

3.5. F-Actin *X*−*Y* Distribution. To date, minimal attention has been given to understanding the subcellular partitioning of GNTs; therefore, we sought to determine whether GNTs altered subcellular compartments in cells after exposure. F-actin is an extremely important and prevalent cytoskeletal protein that has important roles in cell shape, motility, endocytosis, traction force, division, and so on,[44] and its alteration can negatively affect all of these crucial cellular functionalities. Because bulk HeLa cellular uptake levels of US-CNTs and

DOI: 10.1021/acsami.5b04851
ACS Appl. Mater. Interfaces 2015, 7, 14593−14602

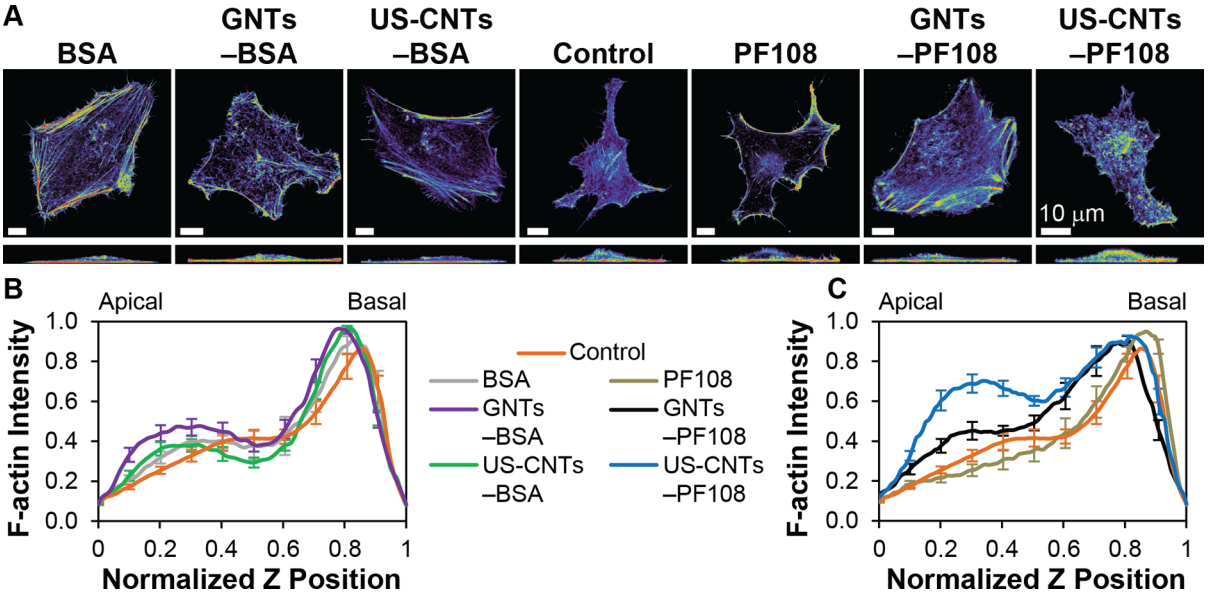

Figure 4. Confocal analysis of $X-Z$ F-actin intensity. (A) $X-Y$ (top) and $X-Z$ (bottom) maximum projections of confocal Z-stacks of rhodamine phalloidin-labeled F-actin in HeLa cells exposed to the indicated conditions for 24 h. $X-Y$ F-actin distributions were similar, although $X-Z$ distributions revealed increased apical intensity for PF108-dispersed US-CNTs and GNTs. All scale bars are 10 μm. (B,C) Quantification of F-actin intensity per pixel as a function of normalized cell Z position for (B) BSA and (C) PF108 samples. BSA and PF108 plots are separated for clarity. n = 11 for control; n = 7 for BSA and PF108; and n = 10 for GNTs–BSA, US-CNTs–BSA, GNTs–PF108 and US-CNTs–PF108. Error bars are standard errors of the mean.

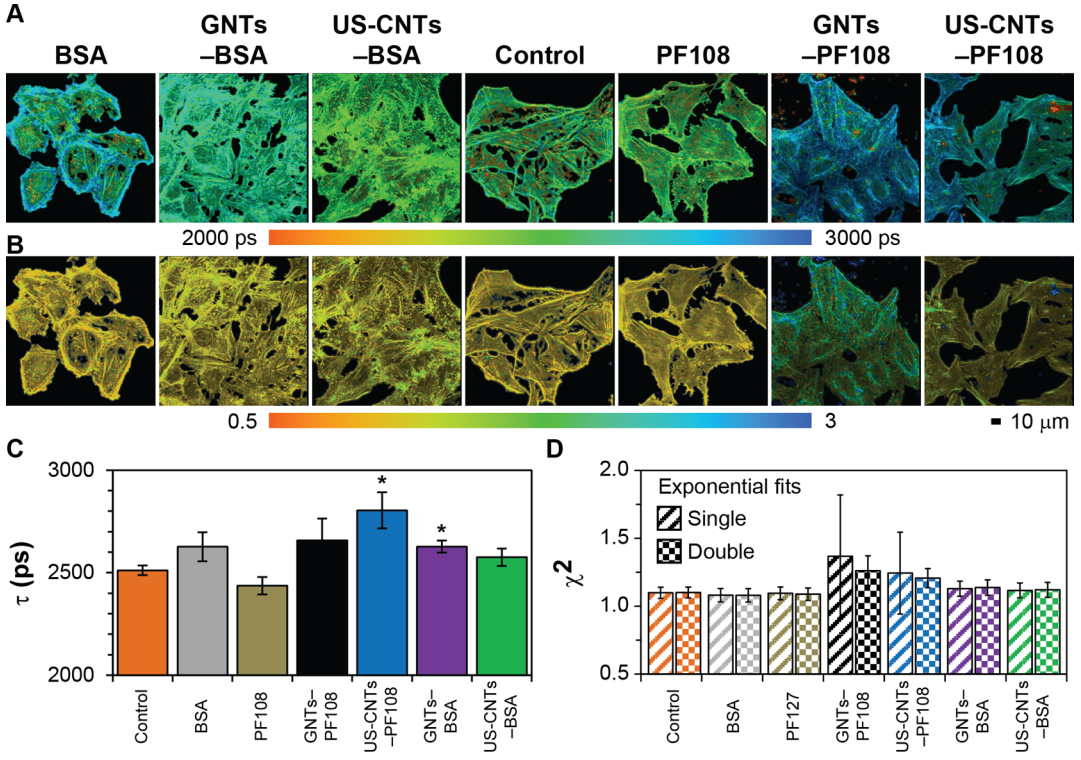

Figure 5. FLIM analysis of F-actin. (A) Heat maps of rhodamine phalloidin fluorescence lifetime (τ) modeled by a single-exponential decay. Note the regions of extreme quenching for the PF108-dispersed US-CNTs and GNTs (red regions). (B) Heat maps of the goodness of fit (χ^2) of fluorescence lifetime for the single-exponential fit. Blue regions for the PF108-dispersed CNTs generally coregister with areas of substantial lifetime quenching and indicate a poor fit by a single exponential only. (C) Quantification of average field of view τ across multiple fields of views. The asterisks indicate statistical significance ($p < 0.05$) compared to control. (D) Quantification of the overall average χ^2 value for fits to both single- and double-exponential decays. Note the large error bars for PF108-dispersed CNTs, which reflect the poor single-exponential fit for the regions of high quenching. n = 14 for control; n = 7 for PF108; n = 6 for BSA; and n = 5 for GNTs–BSA, US-CNTs–BSA, GNTs–PF108, and US-CNTs–PF108. Error bars are the propagation of the standard deviation of the mean for each image to the average of all images per condition.

DOI: 10.1021/acsami.5b04851
ACS Appl. Mater. Interfaces 2015, 7, 14593–14602

GNTs were high (~3 pg/cell) and other types of SWCNTs have previously been shown to interact with and alter F-actin structures,[23,27,45,46] we investigated the potential of these substantially shorter CNTs with different interfacial properties to redistribute cellular F-actin. Widefield fluorescence imaging of rhodamine phalloidin-labeled F-actin of HeLa cells exposed to CNTs revealed little alteration to F-actin structures in the $X-Y$ plane (Figure S6, Supporting Information), although the appearance of a slightly increased supranuclear intensity for the PF108-dispersed CNT samples suggested that there could have been slight alterations to the Z distribution.

3.6. F-Actin $X-Z$ Distribution. Because widefield imaging of HeLa cells suggested the potential for increased apical F-actin intensity and because we previously showed that slightly longer (~145-nm) SWCNTs dispersed with Pluronic F127 alter F-actin structures, especially in the apical Z direction,[23,27,46] we performed confocal imaging of F-actin of HeLa cells exposed to GNTs. We first collected a series of $X-Y$ confocal fluorescence microscopy images through Z, hereafter referred to as Z-stacks, of individual cells exposed to either PF108- or BSA-dispersed US-CNTs or GNTs. Maximum projections in $X-Y$ obtained by compressing the Z-stack images in Z confirmed that the F-actin structures were similar in the plane parallel to the substrate ($X-Y$ plane) (Figure 4A). However, $X-Z$ maximum projections obtained by compressing the Z-stack images in Y revealed higher F-actin intensities per pixel at the apical regions of the cells exposed to PF108-dispersed CNTs (Figure 4A). Quantification of the $X-Z$ intensity confirmed that BSA-dispersed CNTs did not alter the F-actin distribution and demonstrated similar basal cortical F-actin and actin cap signals in HeLa cells compared to controls (Figure 4B). However, HeLa cells exposed to PF108-dispersed US-CNTs and GNTs exhibited slightly altered F-actin Z-intensity distributions (Figure 4C). Further, HeLa cells that were exposed to PF108-dispersed US-CNTs had slightly higher apical intensities than the control for normalized Z positions from ~0.1 to ~0.85. HeLa cells exposed to PF108-dispersed GNTs also showed a similar increase in apical intensity but over a narrower normalized Z position (from ~0.5 to ~0.85).

3.7. FLIM of F-Actin in the Presence of CNTs. Because PF108-dispersed CNTs slightly increased apical F-actin in HeLa cells, we next investigated interactions between CNTs and F-actin. Because the fluorescence lifetime of a fluorophore can change dramatically with alterations to its environment within ~5 nm,[47] we used fluorescence lifetime imaging microscopy (FLIM) to identify any changes in the fluorescence lifetime of rhodamine phalloidin that labeled F-actin to infer a direct interaction between F-actin and CNTs. Figure 5A shows heat maps of the fluorescence lifetime of rhodamine phalloidin of HeLa cells exposed to PF108- and BSA-dispersed CNTs. Although each image showed slight differences in overall lifetime, HeLa cells exposed to PF108-dispersed CNTs had regions of very high quenching (red spots). Quantification of average fluorescence lifetime showed that PF108-dispersed US-CNTs and BSA-dispersed GNTs were significantly different from the control (Figure 5C). However, note that these are average values across all pixels, each of which is a unique data point; therefore, highly quenched regions that represent the most substantial alteration to fluorescence lifetime (e.g., the red regions in the images of cells exposed to PF108-dispersed GNTs) might have ultimately had little effect on the overall average. In addition, the largest difference in average fluorescence lifetime between samples was only 370 ps, representing ~15% of the averages.

Whereas the fluorescence lifetime from HeLa cells exposed to BSA-dispersed CNTs exhibited similar χ^2 values for fits to single- and double-exponential decays, the lifetime for cells exposed to PF108-dispersed CNTs exhibited a slightly higher χ^2 value for a single-exponential decay (Figure 5D). The more dramatic difference was the uncertainty about the mean. The large error bars arose from the regions of dramatic lifetime quenching, as shown in the images of χ^2: Those quenched areas exhibited a high χ^2 value for a single-exponential decay fit of the FLIM data (blue regions), whereas the rest of the image remained best modeled by a single exponential. More details are provided in the Supporting Information.

With regard to the HeLa cell-associated small aggregates of PF108-stabilized US-CNTs and GNTs observed with Raman imaging, our confocal fluorescence and FLIM results suggest that these aggregates were colocalized with apical F-actin structures. These aggregations were mostly absent from HeLa cells exposed to BSA-dispersed CNTs. Interestingly, we observed small pockets of extreme rhodamine phalloidin-labeled F-actin fluorescence lifetime quenching that mimicked the Raman imaging results of intense, punctate PF108-dispersed CNT signal. Therefore, it is likely that aggregates of PF108-dispersed CNTs interacted with HeLa cells at their apical surface, leading to increased F-actin intensity at the apical regions of the cells and resulting in extreme fluorescence lifetime quenching. The fact that these small, apical regions were the only areas of slightly altered F-actin structures suggests that the CNTs had minimal impact on cellular architecture and, thus, vitality. Additionally, because the CNTs either remained well-dispersed or slightly aggregated at the HeLa cell apical regions, it would have been possible for cells to recover or expel associated CNTs upon removal of external CNTs. Cellular recovery from CNT exposure has been previously reported and is considered important for safe cellular applications of CNTs.[21,35,37,38] Overall, these results demonstrate the subcellular interactions of inert GNTs to further the development of GNTs as an MRI CA.

4. CONCLUSIONS

There is a great need for new MRI CAs that can increase contrast while exhibiting minimal toxicity, which would significantly enhance the diagnostic potential of MRI. To that end, we investigated GNTs because of their substantial increase in relaxivities over the current Gd^{3+}-based clinical CAs and other Gd^{3+}-based nanoparticles. Although there have been some studies that have demonstrated that GNTs are not cytotoxic, little attention has been paid to the cellular uptake and subcellular partitioning of GNTs. In this work, we have demonstrated that GNTs stabilized in aqueous solution with two different, clinically relevant dispersing agents, PF108 and BSA, are not acutely cytotoxic and do not reduce cellular proliferation, even though they are internalized at high levels on the order of picograms per cell for human HeLa cells and 1−10 pg/cell for phagocytic macrophage cells. Coregistration of high-resolution phase-contrast images of cells with Raman images that represented local CNT concentrations demonstrated that the CNTs were distributed throughout the cell population, with perinuclear subcellular localization. Raman imaging also revealed that CNTs stabilized with PF108 were slightly more prone to form small aggregates than CNTs dispersed with BSA when administered to HeLa cells. Confocal fluorescence

DOI: 10.1021/acsami.5b04851
ACS Appl. Mater. Interfaces 2015, 7, 14593−14602

imaging and FLIM revealed that the aggregated CNTs slightly increased apical F-actin in cells, but in a manner that was not dependent on whether the CNTs were loaded with Gd^{3+} and that can be mitigated by the dispersing agent. Otherwise, there were no observable changes to gross subcellular morphology. Taken together, these results provide cellular and subcellular information that is essential to advance the development of GNTs as a safe MRI contrast agent for clinical applications.

■ ASSOCIATED CONTENT

Supporting Information

Supporting text: Detailed discussion of PF108- and BSA-dispersed US-CNT and GNT materials characterization and stability, PF108- and BSA-dispersed US-CNT and GNT cellular uptake, and F-actin distribution. Supporting figures: (S1) High-resolution TEM, EDX, and EELS characterization of the GNTs; (S2) materials characterization; (S3) CNT stability; (S4) cellular calcium levels; (S5) Raman imaging of HeLa cells; (S6) widefield F-actin fluorescence images; and (S7) standard curves relating CNT Raman G-band intensity to CNT concentration. The Supporting Information is available free of charge on the ACS Publications website at DOI: 10.1021/acsami.5b04851.

■ AUTHOR INFORMATION

Corresponding Authors

*Phone: 713-348-3268. Fax: 713-348-5155. E-mail: durango@rice.edu (L.J.W.).

*Phone: 412-268-9609. Fax: 412-268-7139. E-mail: krisdahl@cmu.edu (K.N.D.).

*Phone: 412-268-8999. Fax: 412-268-7596. E-mail: mohammad@cmu.edu (M.F.I.).

Author Contributions

M.F.I., K.N.D., and L.J.W. conceived the project. J.J.L. and L.J.W. synthesized the CNTs. B.D.H., K.N.D., and M.F.I. designed the cellular experiments. B.D.H. and P.D.B. performed the experiments. B.D.H., P.D.B., K.N.D., and M.F.I. analyzed the data. B.D.H., K.N.D., and M.F.I. wrote the manuscript. All authors have commented on the manuscript and given approval to the final version of the manuscript.

Notes

The authors declare no competing financial interest.

■ ACKNOWLEDGMENTS

We gratefully acknowledge and thank N. T. Nuhfer and Y. J. Jeong for their assistance with TEM. This work was supported by the National Science Foundation through Grants CMMI-1335417 (M.F.I.), CBET-0954421 (K.N.D.), and CMMI-1300476 (K.N.D.) and through the Graduate Research Fellowship Program (GRFP) 0940902 (J.J.L.), and by the Welch Foundation C-0627 (L.J.W.).

■ REFERENCES

(1) Fauci, A. S., Braunwald, E., Kasper, D. L., Hauser, S. L., Longo, D. L., Jameson, J. L., Loscalzo, J., Eds. *Harrison's Principles of Internal Medicine*, 17th ed.; McGraw-Hill: New York, 2008.

(2) Rinck, P., Ed. *Magnetic Resonance in Medicine. The Basic Textbook of the European Magnetic Resonance Forum*, 7th ed.; TRTF/EMRF, 2013.

(3) Penfield, J. G.; Reilly, R. F. What Nephrologists Need to Know About Gadolinium. *Nat. Clin. Pract. Nephrol.* **2007**, *3*, 654−668.

(4) Ananta, J. S.; Godin, B.; Sethi, R.; Moriggi, L.; Liu, X.; Serda, R. E.; Krishnamurthy, R.; Muthupillai, R.; Bolskar, R. D.; Helm, L.; Ferrari, M.; Wilson, L. J.; Decuzzi, P. Geometrical Confinement of Gadolinium-Based Contrast Agents in Nanoporous Particles Enhances T1 Contrast. *Nat. Nanotechnol.* **2010**, *5*, 815−821.

(5) Laus, S.; Sitharaman, B.; Tóth, É.; Bolskar, R. D.; Helm, L.; Asokan, S.; Wong, M. S.; Wilson, L. J.; Merbach, A. E. Destroying Gadofullerene Aggregates by Salt Addition in Aqueous Solution of $Gd@C_{60}(OH)_x$ and $Gd@C_{60}[C(COOH_2)]_{10}$. *J. Am. Chem. Soc.* **2005**, *127*, 9368−9369.

(6) Laus, S.; Sitharaman, B.; Tóth, É.; Bolskar, R. D.; Helm, L.; Wilson, L. J.; Merbach, A. E. Understanding Paramagnetic Relaxation Phenomena for Water-Soluble Gadofullerenes. *J. Phys. Chem. C* **2007**, *111*, 5633−5639.

(7) Ma, Q.; Jebb, M.; Tweedle, M. F.; Wilson, L. J. The Gadonanotubes: Structural Origin of Their High-Performance MRI Contrast Agent Behavior. *J. Mater. Chem. B* **2013**, *1*, 5791−5797.

(8) Sitharaman, B.; Kissell, K. R.; Hartman, K. B.; Tran, L. A.; Baikalov, A.; Rusakova, I.; Sun, Y.; Khant, H. A.; Ludtke, S. J.; Chiu, W.; Laus, S.; Toth, E.; Helm, L.; Merbach, A. E.; Wilson, L. J. Superparamagnetic Gadonanotubes Are High-Performance MRI Contrast Agents. *Chem. Commun.* **2005**, 3915−3917.

(9) Hartman, K. B.; Laus, S.; Bolskar, R. D.; Muthupillai, R.; Helm, L.; Toth, E.; Merbach, A. E.; Wilson, L. J. Gadonanotubes as Ultrasensitive pH-Smart Probes for Magnetic Resonance Imaging. *Nano Lett.* **2008**, *8*, 415−419.

(10) Tran, L. A.; Krishnamurthy, R.; Muthupillai, R.; da Graça Cabreira-Hansen, M.; Willerson, J. T.; Perin, E. C.; Wilson, L. J. Gadonanotubes as Magnetic Nanolabels for Stem Cell Detection. *Biomaterials* **2010**, *31*, 9482−9491.

(11) Rosenberg, J. T.; Cisneros, B. T.; Matson, M.; Sokoll, M.; Sachi-Kocher, A.; Bejarano, F. C.; Wilson, L. J.; Grant, S. C. Encapsulated Gadolinium and Dysprosium Ions within Ultra-Short Carbon Nanotubes for MR Microscopy at 11.75 and 21.1 T. *Contrast Media Mol. Imaging* **2014**, *9*, 92−99.

(12) Tang, A. M.; Ananta, J. S.; Zhao, H.; Cisneros, B. T.; Lam, E. Y.; Wong, S. T.; Wilson, L. J.; Wong, K. K. Cellular Uptake and Imaging Studies of Gadolinium-Loaded Single-Walled Carbon Nanotubes as MRI Contrast Agents. *Contrast Media Mol. Imaging* **2011**, *6*, 93−99.

(13) Avti, P. K.; Caparelli, E. D.; Sitharaman, B. Cytotoxicity, Cytocompatibility, Cell-Labeling Efficiency, and *in Vitro* Cellular Magnetic Resonance Imaging of Gadolinium-Catalyzed Single-Walled Carbon Nanotubes. *J. Biomed. Mater. Res., Part A* **2013**, *101*, 3580−3591.

(14) Manus, L. M.; Mastarone, D. J.; Waters, E. A.; Zhang, X.-Q.; Schultz-Sikma, E. A.; MacRenaris, K. W.; Ho, D.; Meade, T. J. Gd(III)-Nanodiamond Conjugates for MRI Contrast Enhancement. *Nano Lett.* **2009**, *10*, 484−489.

(15) Miyawaki, J.; Matsumura, S.; Yuge, R.; Murakami, T.; Sato, S.; Tomida, A.; Tsuruo, T.; Ichihashi, T.; Fujinami, T.; Irie, H.; Tsuchida, K.; Iijima, S.; Shiba, K.; Yudasaka, M. Biodistribution and Ultrastructural Localization of Single-Walled Carbon Nanohorns Determined in Vivo with Embedded Gd_2O_3 Labels. *ACS Nano* **2009**, *3*, 1399−1406.

(16) Swierczewska, M.; Rusakova, I.; Sitharaman, B. Gadolinium and Europium Catalyzed Growth of Single-Walled Carbon Nanotubes. *Carbon* **2009**, *47*, 3139−3142.

(17) Avti, P. K.; Talukdar, Y.; Sirotkin, M. V.; Shroyer, K. R.; Sitharaman, B. Toward Single-Walled Carbon Nanotube−Gadolinium Complex as Advanced MRI Contrast Agents: Pharmacodynamics and Global Genomic Response in Small Animals. *J. Biomed. Mater. Res., Part B* **2013**, *101B*, 1039−1049.

(18) Kolosnjaj-Tabi, J.; Hartman, K. B.; Boudjemaa, S.; Ananta, J. S.; Morgant, G.; Szwarc, H.; Wilson, L. J.; Moussa, F. In Vivo Behavior of Large Doses of Ultrashort and Full-Length Single-Walled Carbon Nanotubes after Oral and Intraperitoneal Administration to Swiss Mice. *ACS Nano* **2010**, *4*, 1481−1492.

(19) Gu, Z.; Peng, H.; Hauge, R. H.; Smalley, R. E.; Margrave, J. L. Cutting Single-Wall Carbon Nanotubes through Fluorination. *Nano Lett.* **2002**, *2*, 1009−1013.

DOI: 10.1021/acsami.5b04851
ACS Appl. Mater. Interfaces 2015, 7, 14593−14602

(20) Holt, B. D.; Dahl, K. N.; Islam, M. F. Quantification of Uptake and Localization of Bovine Serum Albumin-Stabilized Single-Wall Carbon Nanotubes in Different Human Cell Types. *Small* **2011**, *7*, 2348−2355.
(21) Holt, B. D.; Dahl, K. N.; Islam, M. F. Cells Take up and Recover from Protein-Stabilized Single-Wall Carbon Nanotubes with Two Distinct Rates. *ACS Nano* **2012**, *6*, 3481−3490.
(22) Holt, B. D.; McCorry, M. C.; Boyer, P. D.; Dahl, K. N.; Islam, M. F. Not All Protein-Mediated Single-Wall Carbon Nanotube Dispersions Are Equally Bioactive. *Nanoscale* **2012**, *4*, 7425−7434.
(23) Holt, B. D.; Short, P. A.; Rape, A. D.; Wang, Y. L.; Islam, M. F.; Dahl, K. N. Carbon Nanotubes Reorganize Actin Structures in Cells and ex Vivo. *ACS Nano* **2010**, *4*, 4872−4878.
(24) Fagan, J. A.; Becker, M. L.; Chun, J.; Hobbie, E. K. Length Fractionation of Carbon Nanotubes Using Centrifugation. *Adv. Mater.* **2008**, *20*, 1609−1613.
(25) Shen, Y.; Jacobs, J. M.; Camp, D. G.; Fang, R.; Moore, R. J.; Smith, R. D.; Xiao, W.; Davis, R. W.; Tompkins, R. G. Ultra-High-Efficiency Strong Cation Exchange LC/RPLC/MS/MS for High Dynamic Range Characterization of the Human Plasma Proteome. *Anal. Chem.* **2004**, *76*, 1134−1144.
(26) Boyer, P. D.; Holt, B. D.; Islam, M. F.; Dahl, K. N. Decoding Membrane- versus Receptor-Mediated Delivery of Single-Walled Carbon Nanotubes into Macrophages Using Modifications of Nanotube Surface Coatings and Cell Activity. *Soft Matter* **2013**, *9*, 758−764.
(27) Holt, B. D.; Shams, H.; Horst, T. A.; Basu, S.; Rape, A. D.; Wang, Y.-L.; Rohde, G. K.; Mofrad, M. R. K.; Islam, M. F.; Dahl, K. N. Altered Cell Mechanics from the Inside: Dispersed Single Wall Carbon Nanotubes Integrate with and Restructure Actin. *J. Funct. Biomater.* **2012**, *3*, 398−417.
(28) Yaron, P.; Holt, B.; Short, P.; Losche, M.; Islam, M.; Dahl, K. Single Wall Carbon Nanotubes Enter Cells by Endocytosis and Not Membrane Penetration. *J. Nanobiotechnol.* **2011**, *9*, 45(01)−45(15).
(29) Duncan, R. R.; Bergmann, A.; Cousin, M. A.; Apps, D. K.; Shipston, M. J. Multi-Dimensional Time-Correlated Single Photon Counting (TCSPC) Fluorescence Lifetime Imaging Microscopy (FLIM) to Detect FRET in Cells. *J. Microsc.* **2004**, *215*, 1−12.
(30) Köllner, M.; Wolfrum, J. How Many Photons Are Necessary for Fluorescence-Lifetime Measurements? *Chem. Phys. Lett.* **1992**, *200*, 199−204.
(31) Ashcroft, J. M.; Hartman, K. B.; Mackeyev, Y.; Hofmann, C.; Pheasant, S.; Alemany, L. B.; Wilson, L. J. Functionalization of Individual Ultra-Short Single-Walled Carbon Nanotubes. *Nanotechnology* **2006**, *17*, 5033.
(32) Liu, J.; Yu, M.; Zhou, C.; Zheng, J. Renal Clearable Inorganic Nanoparticles: A New Frontier of Bionanotechnology. *Mater. Today* **2013**, *16*, 477−486.
(33) Ruggiero, A.; Villa, C. H.; Bander, E.; Rey, D. A.; Bergkvist, M.; Batt, C. A.; Manova-Todorova, K.; Deen, W. M.; Scheinberg, D. A.; McDevitt, M. R. Paradoxical Glomerular Filtration of Carbon Nanotubes. *Proc. Natl. Acad. Sci. U.S.A.* **2010**, *107*, 12369−12374.
(34) Hassan, A. A.; Chan, B. T.-Y.; Tran, L. A.; Hartman, K. B.; Ananta, J. S.; Mackeyev, Y.; Hu, L.; Pautler, R. G.; Wilson, L. J.; Lee, A. V. Serine-Derivatized Gadonanotubes as Magnetic Nanoprobes for Intracellular Labeling. *Contrast Media Mol. Imaging* **2010**, *5*, 34−38.
(35) Jin, H.; Heller, D. A.; Sharma, R.; Strano, M. S. Size-Dependent Cellular Uptake and Expulsion of Single-Walled Carbon Nanotubes: Single Particle Tracking and a Generic Uptake Model for Nanoparticles. *ACS Nano* **2009**, *3*, 149−158.
(36) Jin, H.; Heller, D. A.; Strano, M. S. Single-Particle Tracking of Endocytosis and Exocytosis of Single-Walled Carbon Nanotubes in NIH-3T3 Cells. *Nano Lett.* **2008**, *8*, 1577−1585.
(37) Neves, V.; Heister, E.; Costa, S.; Tîlmaciu, C.; Borowiak-Palen, E.; Giusca, C. E.; Flahaut, E.; Soula, B.; Coley, H. M.; McFadden, J.; Silva, S. R. P. Uptake and Release of Double-Walled Carbon Nanotubes by Mammalian Cells. *Adv. Funct. Mater.* **2010**, *20*, 3272−3279.
(38) Cheng, J.; Fernando, K. A. S.; Veca, L. M.; Sun, Y.-P.; Lamond, A. I.; Lam, Y. W.; Cheng, S. H. Reversible Accumulation of Pegylated Single-Walled Carbon Nanotubes in the Mammalian Nucleus. *ACS Nano* **2008**, *2*, 2085−2094.
(39) Dresselhaus, M. S.; Dresselhaus, G.; Saito, R.; Jorio, A. Raman Spectroscopy of Carbon Nanotubes. *Phys. Rep.* **2005**, *409*, 47−99.
(40) Cherukuri, P.; Gannon, C. J.; Leeuw, T. K.; Schmidt, H. K.; Smalley, R. E.; Curley, S. A.; Weisman, R. B. Mammalian Pharmacokinetics of Carbon Nanotubes Using Intrinsic Near-Infrared Fluorescence. *Proc. Natl. Acad. Sci. U.S.A.* **2006**, *103*, 18882−18886.
(41) Frise, A. E.; Pages, G.; Shtein, M.; Pri Bar, I.; Regev, O.; Furo, I. Polymer Binding to Carbon Nanotubes in Aqueous Dispersions: Residence Time on the Nanotube Surface as Obtained by NMR Diffusometry. *J. Phys. Chem. B* **2012**, *116*, 2635−2642.
(42) Frise, A. E.; Edri, E.; Furó, I.; Regev, O. Protein Dispersant Binding on Nanotubes Studied by NMR Self-Diffusion and Cryo-TEM Techniques. *J. Phys. Chem. Lett.* **2010**, *1*, 1414−1419.
(43) Raoof, M.; Mackeyev, Y.; Cheney, M. A.; Wilson, L. J.; Curley, S. A. Internalization of C_{60} Fullerenes into Cancer Cells with Accumulation in the Nucleus *Via* the Nuclear Pore Complex. *Biomaterials* **2012**, *33*, 2952−2960.
(44) Pollard, T. D.; Earnshaw, W. C. *Cell Biology*, 2nd ed; Elsevier: New York, 2008.
(45) Dulinska-Molak, I.; Mao, H. L.; Kawazoe, N.; Chen, G. P. Variation of Mechanical Property of Single-Walled Carbon Nanotubes-Treated Cells Explored by Atomic Force Microscopy. *J. Biomed. Nanotechnol.* **2014**, *10*, 651−659.
(46) Shams, H.; Holt, B. D.; Mahboobi, S. H.; Jahed, Z.; Islam, M. F.; Dahl, K. N.; Mofrad, M. R. K. Actin Reorganization through Dynamic Interactions with Single-Wall Carbon Nanotubes. *ACS Nano* **2014**, *8*, 188−197.
(47) Berezin, M. Y.; Achilefu, S. Fluorescence Lifetime Measurements and Biological Imaging. *Chem. Rev.* **2010**, *110*, 2641−2684.

DOI: 10.1021/acsami.5b04851
ACS Appl. Mater. Interfaces 2015, 7, 14593−14602